Research Article

Numerical Investigation on Pressure Pulsation Characteristics and Radial Force of a Deep-Sea Electric Lifting Pump at Off-Design Conditions

Yajuan Kang [iD],[1,2,3] **Shaojun Liu** [iD],[2,3,4] **Weisheng Zou** [iD],[5] **and Xiaozhou Hu** [iD][1,3]

[1]*College of Mechanical and Electrical Engineering, Central South University, Changsha 410083, China*
[2]*Shenzhen Research Institute of Central South University, Shenzhen 518000, China*
[3]*National Key Laboratory of Deep Sea Mineral Researches Development and Utilization Technology, 410083 Changsha, China*
[4]*Shenzhen Far East Mineral Exploitation Research Institute Co. Ltd., Shenzhen 518000, China*
[5]*College of Mechanical and Vehicle Engineering, Hunan University, Changsha 410082, China*

Correspondence should be addressed to Shaojun Liu; csu_liushaojun@163.com and Xiaozhou Hu; csu_huxiaozhou@163.com

To predict the vibrational conditions, the generation mechanism, and action law of pressure pulsation and radial force, a computational fluid dynamics (CFD) study of a deep-sea electric lifting pump operating under different off-design conditions was performed. The time-domain and frequency-domain response of the pressure pulsation at different monitoring points and the radial force of impeller distribution were obtained. Differences in pressure pulsation characteristics between the first stage and second stage were observed. The variation law and influential factors of the radial force under different flow rates were discussed. The present investigation shows that the flow field caused by rotor-stator interaction is not uniform, resulting in uneven pressure distribution and pressure pulsation, the combined effects of which produce fluctuating radial forces. Parameters obtained via simulations including head, efficiency, and power, which can reflect the hydraulic performance of the pump, agree well with experimental results; thus, the accuracy of the simulation model and the calculation method was verified. This study provides a basis for improving the structure and reliability of an electric lifting pump.

1. Introduction

The deep sea contains rich mineral resources such as polymetallic nodules, cobalt-rich nodules, and hydrothermal sulfides. [1]. With the depletion of terrestrial mineral resources, the development and utilization of seabed mineral resources has become a hot topic in the international community [2, 3]. The electric lifting pump is a key piece of equipment for deep-sea mining systems and is used to lift mineral resources from the seabed to the mining vessel on the sea surface; it is known as the "heart" of the lifting system [4]. China's self-developed electric lifting pump is a multistage centrifugal pump, the main overcurrent components of which are the impeller and diffuser. Because of the special operational environment and requirements, a conventional pump design method cannot meet the design requirements of an

electric lifting pump. Therefore, the electric lifting pump designed in China adopts an increased flow rate method to widen the flow channel of the impeller such that large particle nodules can smoothly pass through [5]. However, because of the use of the increased flow rate method, the design flow point of the pump deviates from the rated flow point; thus, the pump operates under an off-design condition. When the pump deviates from the design condition, the fluid flow distribution in the impeller is not as uniform as that under design conditions, which leads to pump dynamic instability, and the force acting on the impeller becomes more complex. In addition, the relative movement between the rotating impeller and stationary diffuser, and the circular motion of the medium flow in the diffuser, during off-design conditions may cause the pressure to rapidly fluctuate with time, resulting in pressure pulsation [6]. Pressure pulsation may cause radial

force fluctuation, which will induce vibration and lead to bearing and seal fatigue [7]. The pump outlet pressure pulsation may also cause lifting pipeline resonance, thus seriously affecting the deep-sea mining safety. Therefore, the study of the pressure fluctuation and radial force in the flow field of an electric lifting pump can not only grasp the characteristics of pressure fluctuation and radial force but also effectively prevent failure of the pump caused by the pressure fluctuation and radial force.

The study of the pressure pulsation characteristics and radial force in the centrifugal pump mainly includes two methods: tests and numerical calculations. Because of the high cost, it is difficult to use experimental means to monitor pressure pulsation and radial force in the pump (particularly on rotating blades). In contrast, with the development of CFD technology, calculation of the flow field inside hydraulic mechanicals has now developed into a full three-dimensional (3D) viscous and unsteady stage, and quite in-depth research results have been obtained. Gonzáles et al. [8] numerically studied the pressure fluctuation characteristics of centrifugal pumps and validated the feasibility of numerical simulation via experiments. Guo and Okamoto [9], Li et al. [10], Feng et al. [11], Zhou et al. [12], Dupont et al. [13], and Shi and Tsukamoto [14] studied pressure pulsation and radial force in a centrifugal pump. The results showed that pressure pulsations were caused by rotor-stator interaction. Yao [15], Anish et al. [16], and Jaatinen et al. [17] investigated the influence of the diffuser on the flow field in the pump and found that the internal flow field of the centrifugal pump was mainly affected by rotor-stator interaction. Yuan and Ni [18] studied the clocking effect on pressure fluctuation in a centrifugal pump under off-design conditions and concluded that the effect of diffuser clocking on the pressure pulsation intensity in a centrifugal pump was more obvious. Solis et al. [19] studied the flow characteristics in the rotating impeller region and concluded that the pressure fluctuation frequency was exactly the blade frequency under different flow rates. Esch et al. [20] performed numerical calculations to predict the radial force of a centrifugal pump with different impeller outer diameters and compared the calculation results to the experimental results, and they showed good agreement. Barrio et al. [21] studied the radial force distribution of a centrifugal pump impeller using theoretical, numerical, and experimental methods and concluded that the radial force under a nondesign condition was greater than that under a design condition. Gonzalez et al. [22] studied the radial force characteristics of an impeller under different tongue gap conditions and found that the change in the gap at the tongue had a great influence on the radial force. Yang et al. [23] studied the radial force of a centrifugal pump and found that the radial force distribution of the impeller is not uniform, and the phase change of the impeller is unstable.

The aforementioned works on pressure fluctuation and radial force of a centrifugal pump mostly focused on the single-stage centrifugal pump or one stage of the multistage centrifugal pump. Research regarding interference phenomenon between the rotating impeller and static diffuser in the multistage centrifugal pump is not sufficiently comprehensive, and the influence from stage to stage is not considered, which leads to an insufficient understanding of the internal flow characteristics of the pump as a whole. In addition, up to now, there have been limited research studies regarding deep-sea electric lifting pumps, particularly research on the pressure pulsation characteristics and radial force under nondesign conditions and the characteristics of the interaction between the stages.

In this study, the 3D unsteady flow field of a two-stage electric lifting pump was calculated. After being verified by hydraulic performance tests, the CFD model was utilized to predict pressure pulsation and radial force of the multistage electric lifting pump. The pressure pulsation during the first stage and second stage was compared, and the variation law and influential factors of the radial force under different flow conditions were discussed. The present work can provide a theoretical basis for further study of transient characteristics and structural optimization of a deep-sea electric lifting pump.

2. Numerical Method

2.1. Calculation Models. A two-stage electric lifting pump was selected as the calculation model. According to the requirement of a 1000 m pilot marine test system developed by the China Ocean Mineral Resources R&D Association (COMRA), the rated flow rate of the electric lifting pump is 420 m^3/h, the density of the nodule is 2000 kg/m^3, and the maximum particle size of nodules is 20 mm. To allow the coarse particles to smoothly pass through the electric lifting pump, the increased flow rate method was applied to design the pump, which can widen the flow channel; however, this method can cause the flow design point to be at the rated operating point. The rotating speed n was 1450 rpm, the design flow rate Q was 800 m^3/h, and the single-stage head H was 40 m. The overall structure of the two-stage lifting motor pump is shown in Figure 1. A two-dimensional (2D) illustration of the electric lifting pump stage is shown in Figure 2. The specification and main geometric parameters are shown in Table 1.

2.2. Simulation Domain and Mesh Generation. 3D modeling of a two-stage electric lifting pump was performed using Pro/E. To avoid the influence of the inlet vortex zone on the flow field and flow rate, a section of the inlet pipe was added at the impeller inlet; considering the influence of the outlet boundary condition on the diffuser outlet and convergence, a section of the outlet pipe was added at the diffuser outlet. The simulation domain is shown in Figure 3.

The mesh of the intake pipe, impellers, diffusers, and discharge pipe was generated using the commercial software ANSYS 18.0 module ICEM. To facilitate discrete equation convergence and more accurately solve the pressure gradient, meshes for all the components were created using hexahedral cells as shown in Figure 4. To improve the fitness of the grid, the mesh was locally refined in the near-wall area. To meet the requirements of the shear stress transport (SST) k-ω turbulence model, the $Y+$ value was maintained near 1.0 in accordance with the suggestion in the literature, and good numerical resolution was ensured in the boundary layer [24]. A grid independence verification for a two-stage electric lifting pump simulation was performed considering the six
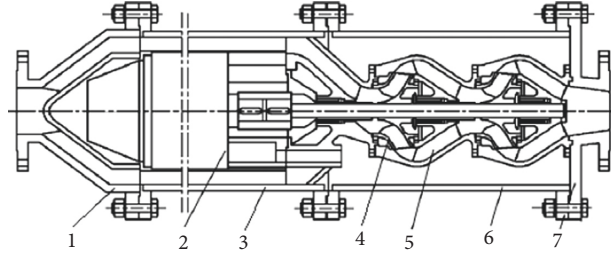
FIGURE 1: Overall structure of the two-stage electric lifting pump. 1, inlet flange; 2, motor; 3, motor cylinder body; 4, impeller; 5, diffuser; 6, pump cylinder body; 7, outlet flange.
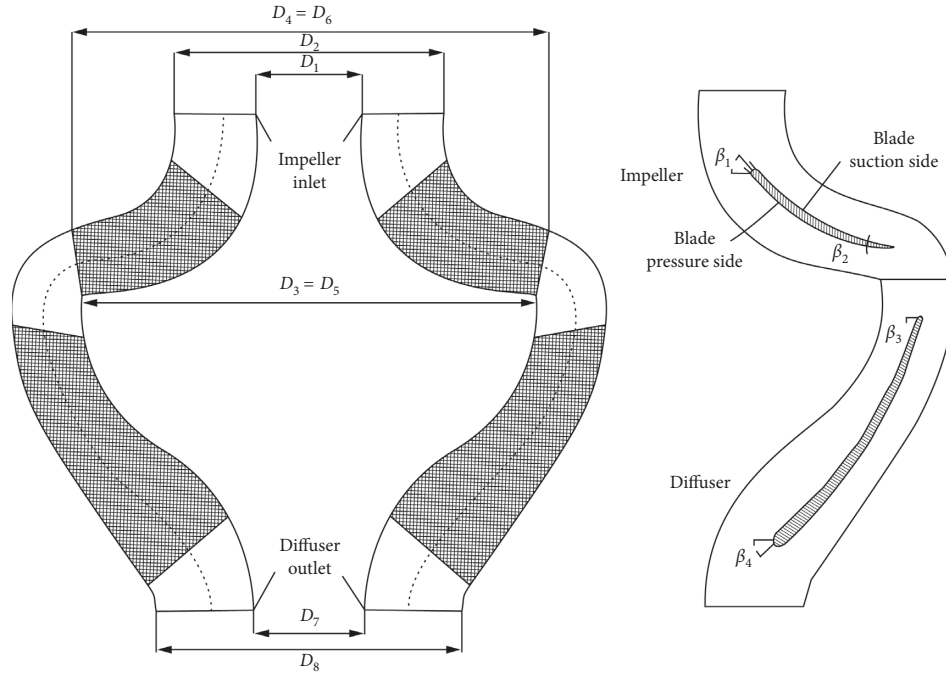

FIGURE 2: 2D illustration of the electric lifting pump stage.

levels of grid refinement as listed in Table 2. To improve the calculation efficiency without reducing the calculation precision, the head of the rated flow point at less than 1% was used as the indicator of grid independence verification [25, 26]. As shown in Table 2, fluctuations in the head are small when the number of grids is greater than 5.2 million. Considering the configuration and calculation time of the computer, the grid numbers for the different components were as follows: impeller, 1,012,468; diffuser, 1,365,458; and inlet and outlet, 261,217.

2.3. Monitoring Points.
To analyze the pressure pulsation characteristics, different monitoring points were set on the pressure side and suction side of the adjacent flow channels of the first stage impeller blades, respectively, as shown in Figure 5(a). Figure 5(b) shows the monitoring points on the diffuser blades, from which it can be seen that monitoring points D_{11}, D_{12}, D_{13}, D_{14}, and D_{15} are set along the flow direction. Similarly, the monitoring points were set to the same position inside the second stage marked with the lower corner "2."

2.4. Governing Equations.
The Reynolds-averaged Navier–Stokes equations were applied for the calculation of the flow field inside the electrical lifting pump as follows [27]:

(1) Continuity equation:

$$\frac{\partial(\rho)}{\partial t} + \frac{\partial(\rho u_i)}{\partial x_i} = 0. \tag{1}$$

(2) Momentum equation:

$$\frac{\partial \rho_i}{\partial t} + \frac{\partial(\rho_i u_j)}{\partial x_j} = -\frac{\partial P}{\partial x_i} + \frac{\partial}{\partial x_j}\left[\mu\left(\frac{\partial u_i}{\partial x_j} + \frac{\partial u_j}{\partial x_i}\right)\right.$$
$$\left. + \mu_t\left(\frac{\partial \overline{u}_i}{\partial x_j} + \frac{\partial \overline{u}_j}{\partial x_i}\right) - \frac{2}{3}\left(\rho k + \mu_t\frac{\partial \overline{u}_i}{\partial x_j}\right)\delta_{ij}\right] + F_i, \tag{2}$$

where μ is the dynamic viscosity, F_i is the source item, k is the turbulent kinetic energy, and μ_t is the turbulent viscosity.

TABLE 1: Main specifications and geometric parameters.

Description	Parameter	Value
Rated flow rate	Q_r (m³/h)	420
Design flow rate	Q_d (m³/h)	800
Stage	S	2
Total head	H (m)	80
Single-stage head	H_s (m)	40
Rotating speed	n (rpm)	1450
Specific speed	n_s	157
Length of the two-stage electric lifting pump	L (mm)	5739
Impeller	Inlet inlet diameter D_1 (mm)	85
	Outlet inlet diameter D_2 (mm)	390
	Inlet outlet diameter D_3 (mm)	240
	Outlet outlet diameter D_4 (mm)	408
	Inlet blade angle β_1	29°
	Outlet blade angle β_2	21°
	Outlet blade width b_2 (mm)	75
	Blade number Z_1	3
Diffuser	Inlet inlet diameter D_5 (mm)	390
	Outlet inlet diameter D_6 (mm)	85
	Inlet outlet diameter D_7 (mm)	550
	Outlet outlet diameter D_8 (mm)	240
	Inlet blade angle β_3	12°
	Outlet blade angle β_4	85°
	Vane number Z_2	4

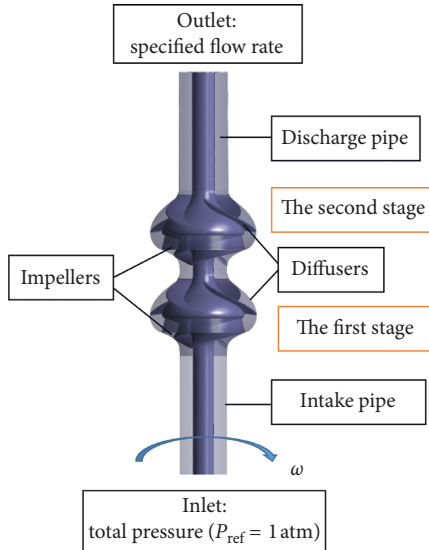Several dimensions are shown in Figure 2.

FIGURE 3: Generic representation of the simulation domain.

2.5. Boundary Condition and Solution Method. The inlet boundary was set as the total pressure with the reference pressure 1 atm, and the turbulent density of the inlet was set to 5%; the outlet was set as the mass flow. The impeller was calculated in a rotating coordinate system in a multi-coordinate system, and the remainder of the flow passages was calculated in a stationary coordinate system. The SST *k*-*ω* turbulence model combines the merits of the *k*-*ω* turbulence model and the *k*-*ε* turbulence model in the boundary layer calculations and has good calculation accuracy, as suggested by Ofuchi. Thus, it was chosen as the calculation model in this work [28, 29]. In the unsteady calculation, the dynamic and static components were coupled using a transient rotor-stator method and the steady calculation results were taken as the initial conditions for the unsteady calculation. The governing equations were spatially discretized based on the finite volume method. The time discretization adopts the second-order full implicit scheme. The unsteady time step was set to 4.597×10^{-4} s, corresponding to the changed angle of 4° of the impeller rotation. For accuracy analysis, 10 cycles were calculated, and the data of the last cycle were analyzed. The convergence criterion was set to 10^{-5}.

3. Experimental Verification

To verify the calculation accuracy, the head, power, and efficiency of the two-stage electric lifting pump under different flow rates were numerically predicted and compared to the corresponding experimental results. Complete hydraulic performance experiments were carried out on a test bench for the two-stage electric lifting pump, as shown in Figure 6. The test device, conditions, methods, and data were all in accordance with the requirements of the acceptance test for hydraulic performance of a rotary power pump GB/T 3216-2016 [30].

The test device was mainly composed of an electric lifting pump, test pipelines, and a stabilization pipe. The test instrument was composed of an electromagnetic flow meter, a pressure transmitter, and a hydraulic mechanical comprehensive tester. A change in the working point was realized by
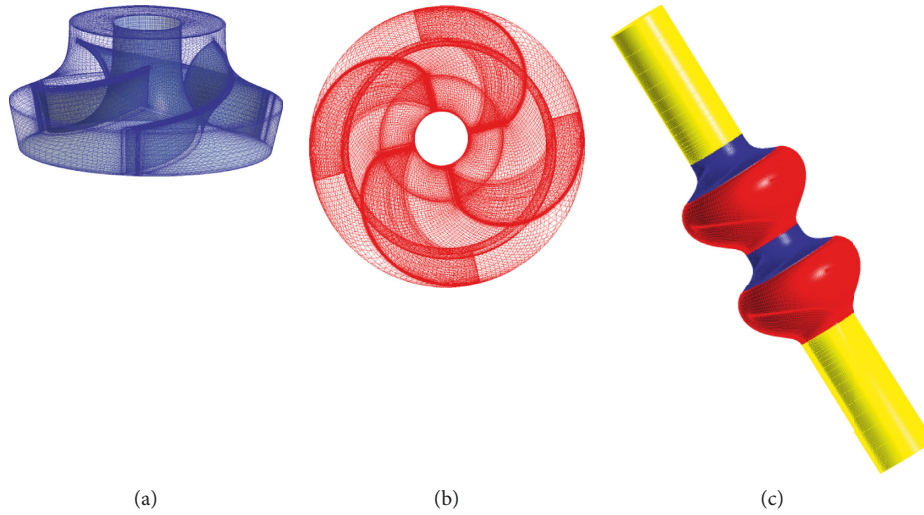
(a) (b) (c)

FIGURE 4: Computational grids used for the electric lifting pump: (a) impeller, (b) diffuser, and (c) two-stage model.

TABLE 2: Grid independence analysis ($Q = 420\,\text{m}^3/\text{h}$; $n = 1450\,\text{rpm}$).

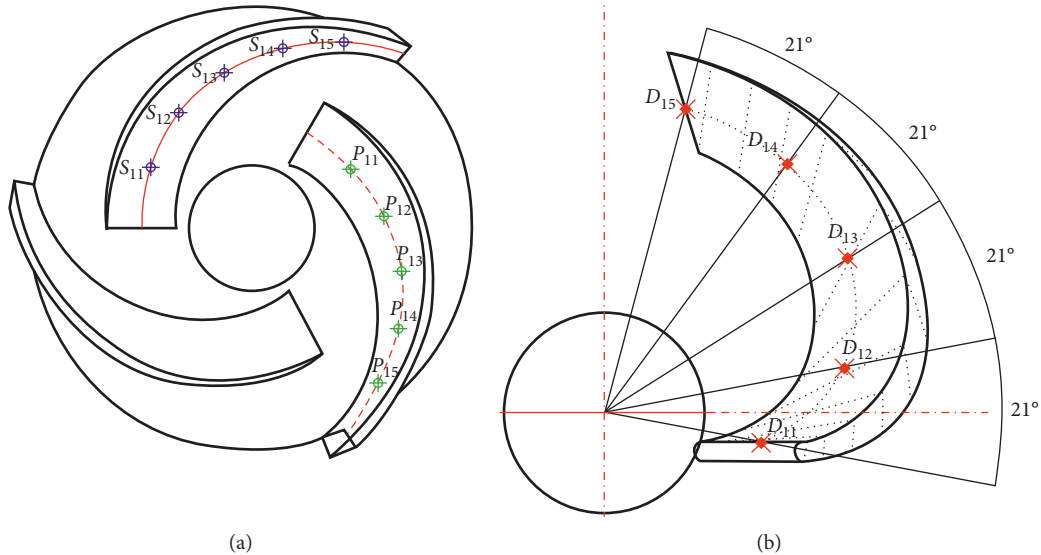| Grid	Impeller	Diffuser	Inlet and outlet	Total (two stages)	Head (m)
1	388455	504336	324512	2110094	87.14
2	562764	788689	432589	3135495	88.48
3	863458	1097513	467894	4389836	89.57
4	1012468	1365458	522434	5278286	89.75
5	1413368	1545079	625603	6542497	89.81
6	1732435	1887846	651450	7892012	89.89

(a) (b)

FIGURE 5: Monitoring point positions inside the (a) impeller and (b) diffuser.

adjusting the opening of the regulating valve in the outlet pipeline. The pump was tested at a speed of 1450 rpm.

Figure 7 shows a comparison between the numerical results and experimental results at different flow rates. The simulation values were consistent with the overall trends of the experimental values. Specifically, the head of the pump obtained via the numerical simulations was slightly higher than that via the experiments, and the relative error (relative error is the ratio of the difference between the simulated value and the experimental value to the experimental value)
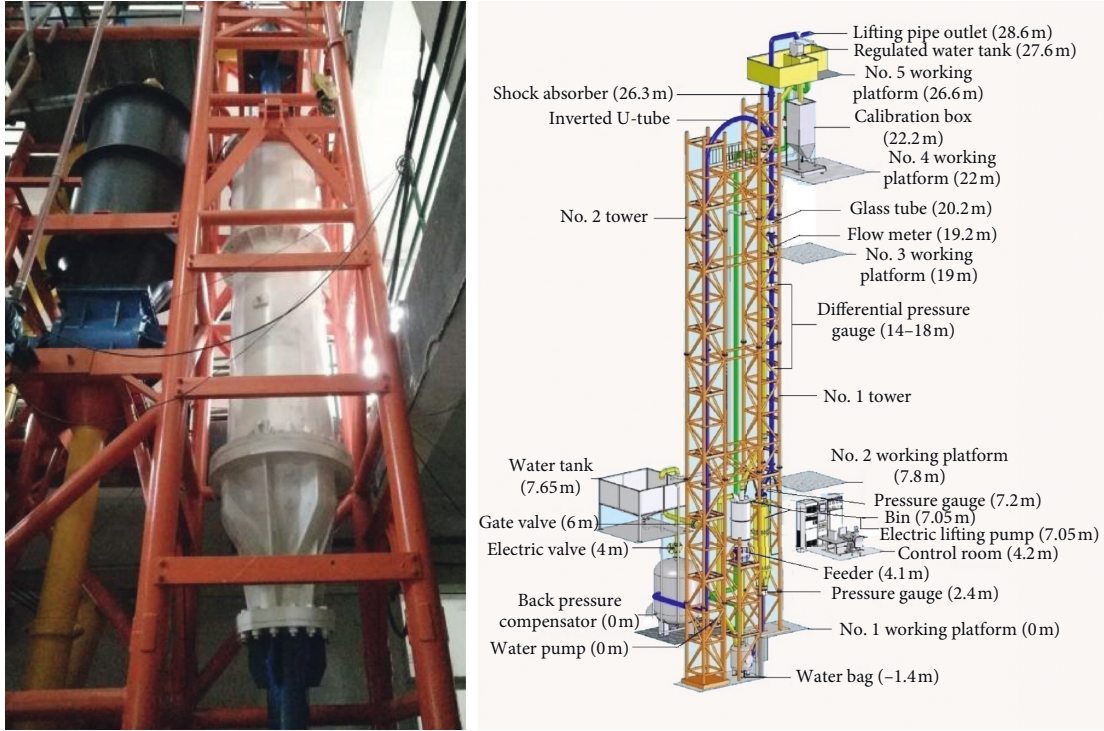
Figure 6: Two-stage electric lifting pump experimental system.

was no greater than 4.5%, while the design flow point was 3.1%; however, the simulated efficiency at a small flow point was slightly larger than the experimental value, and the relative error was no greater than 10%, while the design flow point was 2.9%. Therefore, it can be concluded that the numerical method and model can accurately predict the hydraulic performance characteristics of the electric lifting pump. Their correctness can be verified and provide a guarantee for further investigations regarding pressure fluctuation and impeller radial force.

4. Results

4.1. Pressure Pulsation. In real industrial applications, because the impeller is rotating at a high speed and the diffuser is stationary, a so-called rotor-stator interaction phenomenon occurs, which is the main reason for the pressure pulsation in the pump. For the rated flow rate, the static pressure distribution at $z = 170$ mm (this section is the position of the impeller outlet and the diffuser inlet) with different time steps is shown in Figure 8. It is shown that because of the interaction between the rotor and stator, as the impeller blade is near the diffuser blade, the static pressure in the edge of impeller blade and the corresponding passage significantly increases, resulting in an uneven static pressure distribution. The combined action of these fluctuating pressures produces the fluctuating radial force of the fluid. Therefore, to study the fluid radial force inside the pump, the pressure pulsation inside the pump needs to be analyzed.
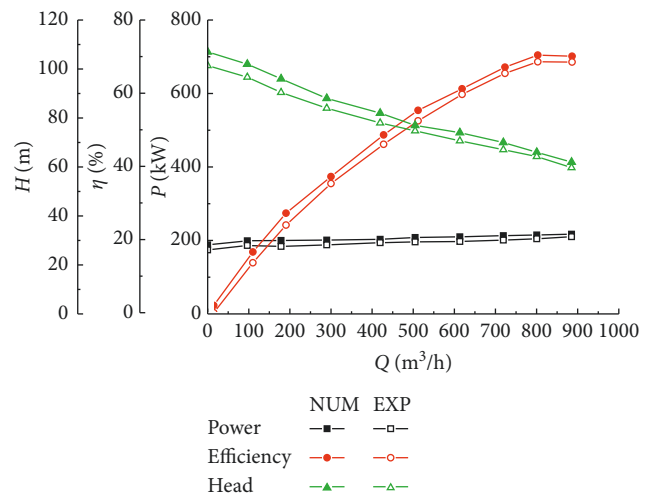

Figure 7: Characteristic curves of the two-stage electric lifting pump.

To analyze the pressure pulsation, the pressure pulsation coefficient C_p was used to measure the magnitude of the pressure pulsation as follows:

$$C_p = \frac{P - \overline{P}}{0.5\,\rho u^2}, \tag{3}$$

where P is the static pressure at the position of the monitoring point, $\overline{P}$ is the average pressure of the impeller in one rotation period, ρ is the water density, and u is the peripheral speed of the impeller outlet.
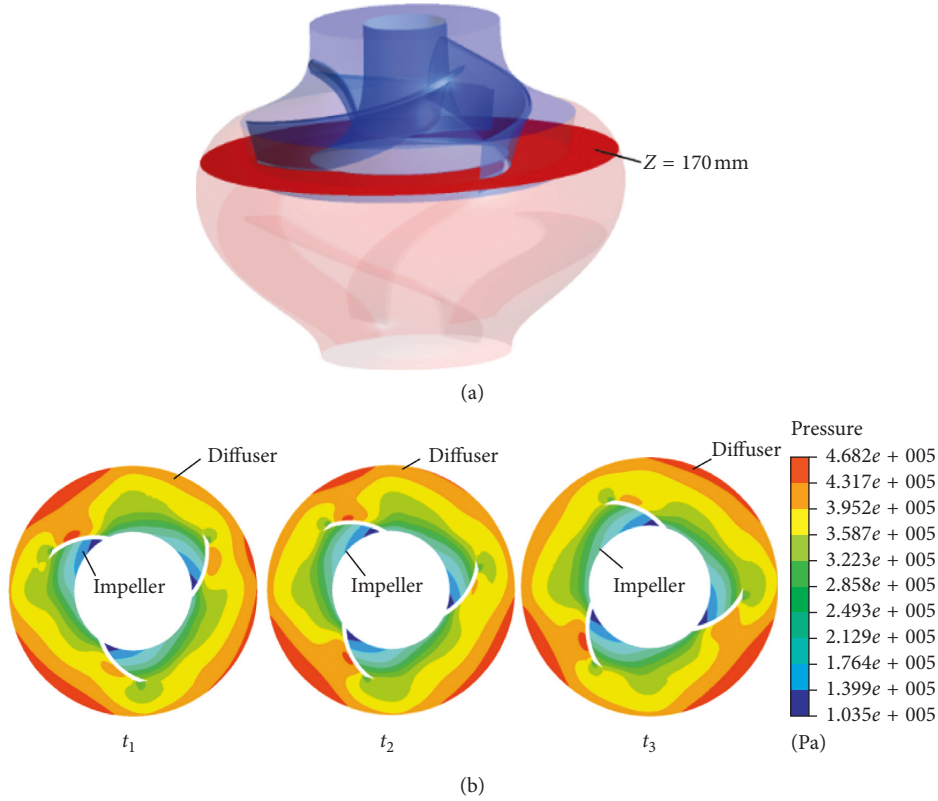
(a)

(b)

FIGURE 8: Static pressure distribution at (a) $z = 170$ mm (this section is the position of the impeller outlet and the diffuser inlet) and (b) different time steps.

Figures 9(a) and 9(b) show that the pressure pulsation of monitoring points in the impeller is periodic in the first-stage impeller. When the impeller blade sweeps the diffuser blade, there is a significant pressure fluctuation in the impeller. Four similar waveforms appear in one cycle, which is equal to the number of diffuser blades. The pressure pulsation from the impeller inlet to the outlet gradually increases, and the pressure pulsation excitation is from the impeller outlet. The medium at the impeller outlet has a higher velocity and exchanges energy with the diffuser inlet, resulting in the largest pressure pulsation amplitude occurring at the impeller outlet. Figure 9 shows that the monitoring points P_{11}, S_{11}, P_{12}, and S_{12} near the impeller inlet have two troughs, indicating that the inlet pressure is not very stable. Comparing Figures 9(a) and 9(b), it can be seen that the pressure pulsation intensity on the blade pressure side is greater than that on the suction side.

Figure 9(c) shows the pressure pulsation time domain of the monitoring points in the diffuser. There are three similar pressure waveforms in one cycle, and there are two peaks at the monitoring point D_{11} near the diffuser inlet, indicating that the diffuser inlet pressure is unstable mainly because the rotating impeller produces axial frequency pulsation on the stationary diffuser, that is, dynamic and static coupling between the impeller and diffuser results in pressure pulsation. The pressure fluctuations near the diffuser inlet are more severe than those in other positions. The pressure pulsation amplitude from the inlet to the outlet of the diffuser gradually decreases, which indicates

that the impeller outlet and diffuser inlet are the main excitation source of the pressure pulsation; the pulsation excitation is continuously attenuated as it moves away from the boundary between the impeller and diffuser.

Figure 10 shows the time-domain diagrams of monitoring points during the second stage. During the second stage, the flow channel periodically changes as during the first stage. The amplitude of the pulsation coefficient in the impeller gradually increases from the impeller inlet to the impeller outlet, while the diffuser gradually decreases from the inlet to the outlet. However, the amplitude of the pressure pulsation coefficient of each monitoring point during the second stage is greater than that of the first stage, indicating that the flow channel of the second stage is affected not only by its own rotor-stator interaction but also by the first-stage flow channel in the front; thus, the excitation is superimposed.

To further analyze the pressure pulsation of the impeller and diffuser, fast Fourier transform was applied to show the unsteady pressure features in the frequency domain. Equation (4) was used to calculate the blade passing frequency f_{ib} as follows:

$$f_{ib} = \frac{n}{60} \times Z, \tag{4}$$

where n is the speed and Z is the blade number.

The impeller speed is 1450 r/min, the impeller frequency f_i is 24 Hz, and the impeller blade frequency f_{ib} is 72 Hz. Figures 11(a) and 11(b) show that the main frequency of the
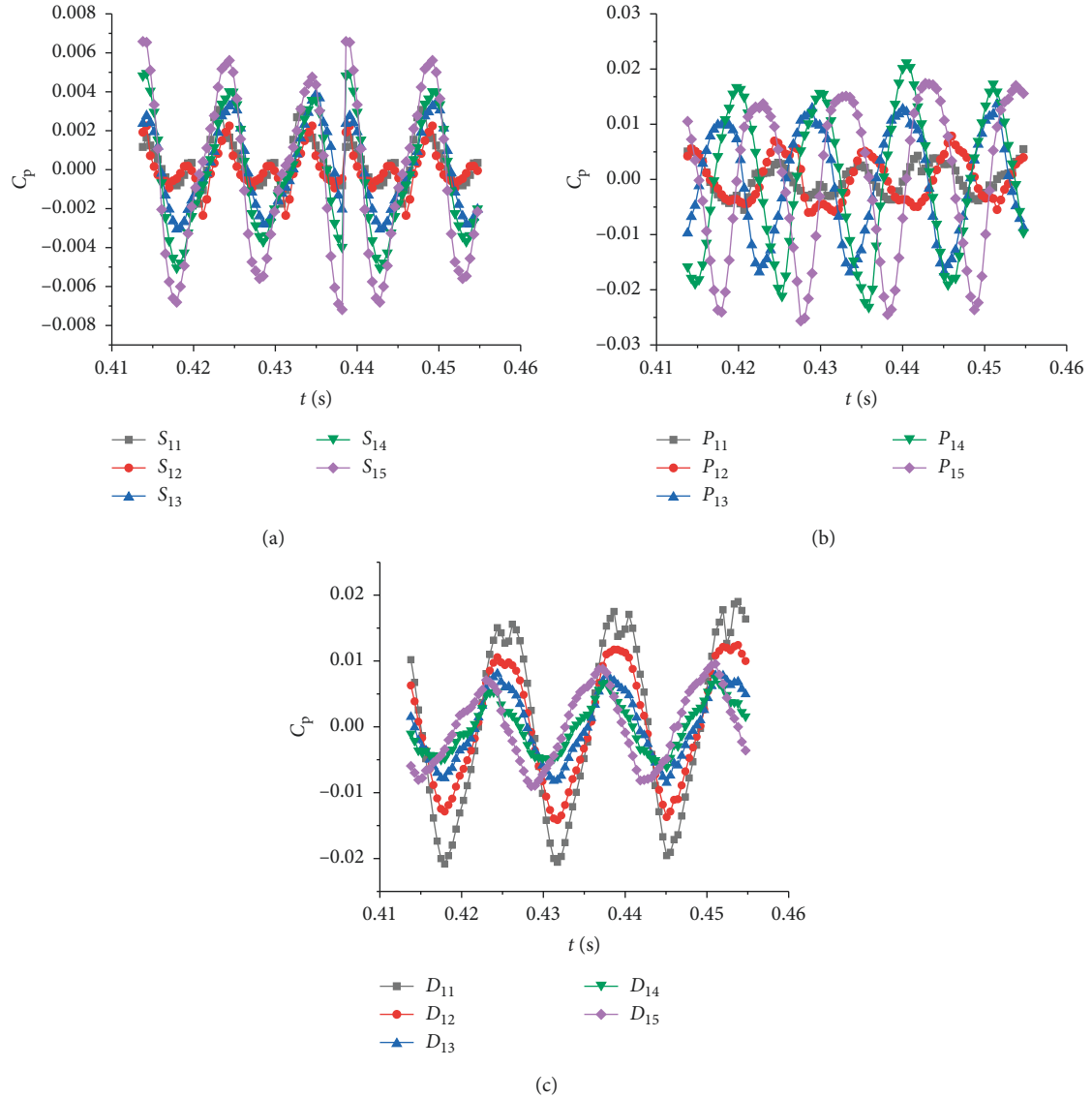
(a)

(b)

(c)

Figure 9: Pressure pulsation time-domain diagram of the first stage: (a) impeller blade suction side, (b) impeller blade pressure side, and (c) diffuser.

pulsation signal of the monitoring points in the impeller has the same value of 96 Hz, that is, 4 times the impeller frequency, which is exactly equal to the number of diffuser blades. This phenomenon shows that the pressure pulsation in the impeller is closely related to the frequency of the impeller and number of diffuser blades. Figure 11(c) shows that the main frequency of the pulsation excitation at the monitoring points in the diffuser is 72 Hz, which is consistent with the impeller blade frequency.

The pressure pulsation frequency of the internal monitoring points of the secondary diffuser is one-time f_{ib}, which is similar to the frequency domain distribution of the first-stage diffuser. However, at each monitoring point in the secondary diffuser, the pressure also fluctuated significantly at 2 times f_{ib} and 3 times f_{ib}, as shown in Figure 12(c), mainly because the secondary diffuser was not only affected by the blade frequency of the secondary impeller but also the first-

stage flow passage. Moreover, the first diffuser has a swirling flow, while the secondary diffuser outlet has a free outflow. The different outflow conditions of the two-stage vane result in a certain difference in the frequency distribution between the diffusers during the first and second stages.

4.2. Radial Force. The radial force is primarily attributed to the unstable pressure distribution at the impeller outlet resulting from the nonuniform flow field and rotor-stator interactions.

The streamline distribution for different flow rates is shown in Figure 13. The circumfluence and vortices in the trailing edge of the impeller and diffuser can be clearly observed under off-design conditions. The smaller the flow rate, the more turbulent the flow. The unsteady flow field in the pump affects the pressure distribution on the solid
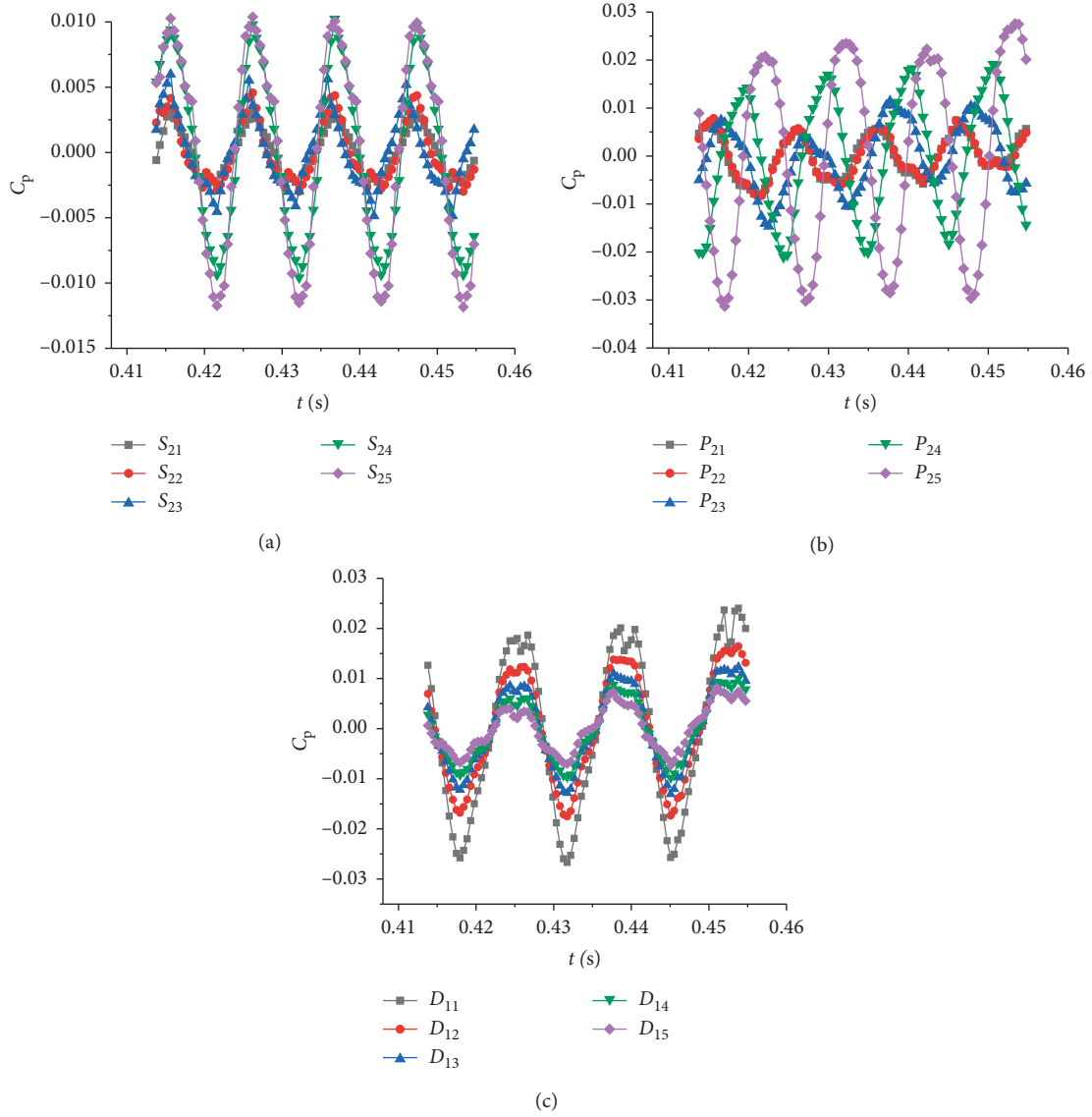
FIGURE 10: Pressure pulsation time-domain diagram of the second stage: (a) impeller blade suction side, (b) impeller blade pressure side, and (c) diffuser.

surface of the impeller which changes over time, as shown in Figure 14.

Because of the relative motion between the high-speed rotating impeller and the static diffuser, the pressure distribution along the circumferential direction is obviously asymmetrical (as shown in the black box area). As the flow rate decreases, the pressure distribution is increasingly uneven. From a geometrical perspective, this is because of a mismatch between the liquid flow angle and diffuser inlet angle under nondesign conditions, which exacerbates the rotor-stator interference between the impeller and the diffuser.

Assuming that the area of each grid node is equal and the static pressure at each grid node is uniformly distributed, the forces acting on each node in all directions can be solved. Then, the magnitude and direction of the total forces can be obtained through the force synthesis theorem. The radial force acting on the impeller can be obtained

according to the following equations in the numerical simulations [6, 31, 32]:

$$F_i = P_i \left(\frac{2\pi R_2 D_2}{N} \right), \tag{5}$$

$$F_i^x = -F_i \left(\frac{x_i}{R_2} \right),$$
$$F_i^y = -F_i \left(\frac{y_i}{R_2} \right), \tag{6}$$

$$F_x = \sum_{i=1}^{N} F_i^x,$$
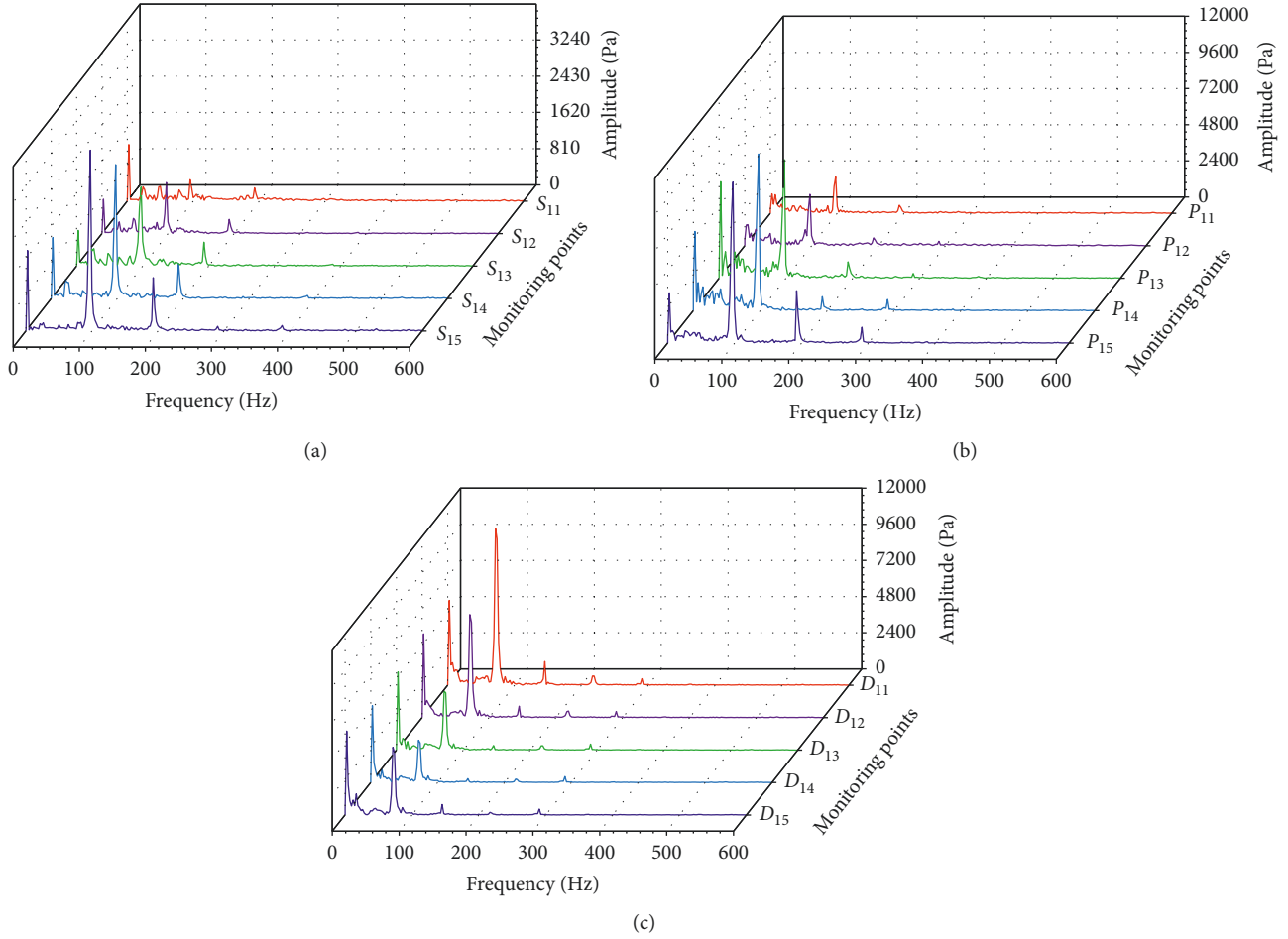$$F_y = \sum_{i=1}^{N} F_i^y, \tag{7}$$

(a)

(b)

(c)

FIGURE 11: Pressure pulsation in the frequency domain at monitoring points during the first stage: (a) impeller blade suction side, (b) impeller blade pressure side, and (c) diffuser.

$$F = \sqrt{F_x^2 + F_y^2},$$

$$\alpha = \arctan\left(\frac{F_x}{F_x}\right),$$

(8)

where N is the number of grid nodes on the coupling surface; P_i is the pressure of the i-th grid node; F_i is the pressure of the tiny area of the i-th grid node; F_i^x and F_i^y are the components of the pressure of the tiny region of the i-th mesh node in the x-axis and y-axis directions, respectively; F_x and F_y are the components of total radial force F in the x-axis and y-axis directions, respectively; R_2 is the impeller radius; D_2 is the flange outlet diameter; and alpha is the angle between the radial force and x direction.

Figure 15 shows the polar coordinate diagram of the radial force on the impellers of the two-stage electric lifting pump under four different flow rates. The circumferential coordinates represent the angle of the impeller rotation during a rotating period, while the length of the connecting line from the center of the circle to a point on the curve represents the radial force at a certain moment. Figure 15 shows the radial force decreases with an increase in flow rate. When $Q = 200\,\mathrm{m^3/h}$, the radial force of the impeller is approximately twice that of the designed flow condition

because the velocity and pressure distribution of the liquid around the impeller is more uneven when the pump operates under nondesign conditions, thus resulting in a larger radial force. The distribution of the radial force under different flow conditions is basically the same and all show a certain periodicity. The rotor-stator interference between the impeller and diffuser has a significant influence on the radial force. When a blade of the impeller passes over the vane blade, a certain degree of radial force pulsation occurs. The transient radial force is the most unstable at $Q = 200\,\mathrm{m^3/h}$. This phenomenon easily causes unstable rotor operation. At the rated working point, the radial force is smaller and the fluctuation is more regular than at a flow rate of $200\,\mathrm{m^3/h}$. The transient radial force under design conditions has the strongest regularity and thus the smallest fluctuation.

For the same flow rate, the radial force on the secondary impeller is greater than that on the first impeller, and the fluctuation is stronger. This is because of the uneven distribution of the flow pattern at the outlet of the first impeller, which will further deteriorate when it propagates to the next stage. Therefore, it can be easily inferred that the secondary impeller is strongly affected by the interference effect.

Figure 16 shows a radial force vector diagram of the impeller in a rotating cycle under different flow conditions.
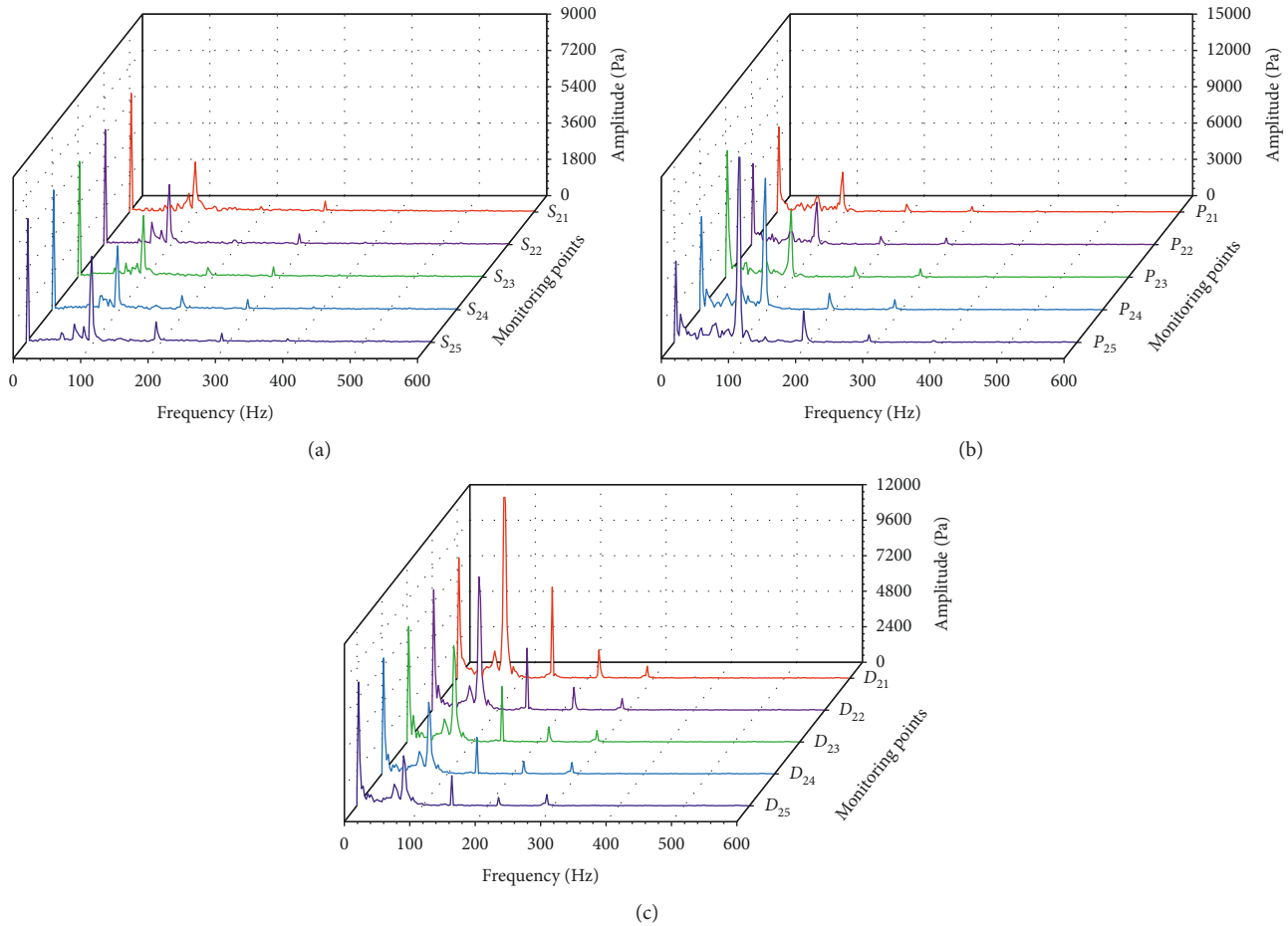
(a)

(b)

(c)

FIGURE 12: Pressure pulsation in the frequency domain at monitoring points during the second stage: (a) impeller blade suction side, (b) impeller blade pressure side, and (c) diffuser.

The vector coordinate of a point in the figure represents the magnitude and direction of the radial force at a certain moment. The impeller center coordinates are (0, 0). The radial force distinctly changes both in magnitude and direction as the impeller rotates. Under different flow rates, the distribution of the radial force vectors is similar, a triangle-like distribution. Each lap corresponds to a change period in the radial force and each peak point represents a rotor-stator interference between the impeller and the diffuser. Because the number of impeller blades is 3 and the number of diffusers is 4, the impeller and the diffuser interfere 12 times during a cycle of impeller rotation, resulting in 12 peak points. The structure of the impeller and diffuser and the rotor-stator interference is related to the radial force. The action law and induction mechanism of the radial force of the unsteady fluid in the pump can be explained as follows: the vectors vary in size and direction, which indicates that the radial force acting on the impeller is unstable. When the flow rate is less than the rated point, the center of the vector force distribution deviates from the axis and the impeller is eccentrically subjected to radial force. Therefore, considering the pump system stability, it is preferably avoided to operate at less than the rated condition for a long time period.

5. Conclusions

In this study, the pressure pulsation characteristics and radial forces in a two-stage electric lifting pump for deep-sea mining were studied. The numerical simulation method was first validated by external characteristic tests, and then the pressure pulsation characteristics at the same position during the first and second stages were analyzed. Finally, the radial force under different flow rates was compared. The main conclusions are as follows:

First, the time-domain characteristics of the pressure pulsation during the first and second stages of the pump are similar. The amplitude of the impeller pressure pulsation coefficient gradually increases from the inlet to outlet, while the pressure pulsation coefficient amplitude in the diffuser gradually decreases from the inlet to outlet. Energy exchange between the impeller and diffuser results in the largest pressure pulsation coefficient occurring at the impeller outlet. The monitoring points on the impeller blades show four similar waveforms during one cycle, consistent with the number of diffuser blades. The monitoring points on the diffuser blades show three similar waveforms during one cycle, which is consistent with the number of impeller
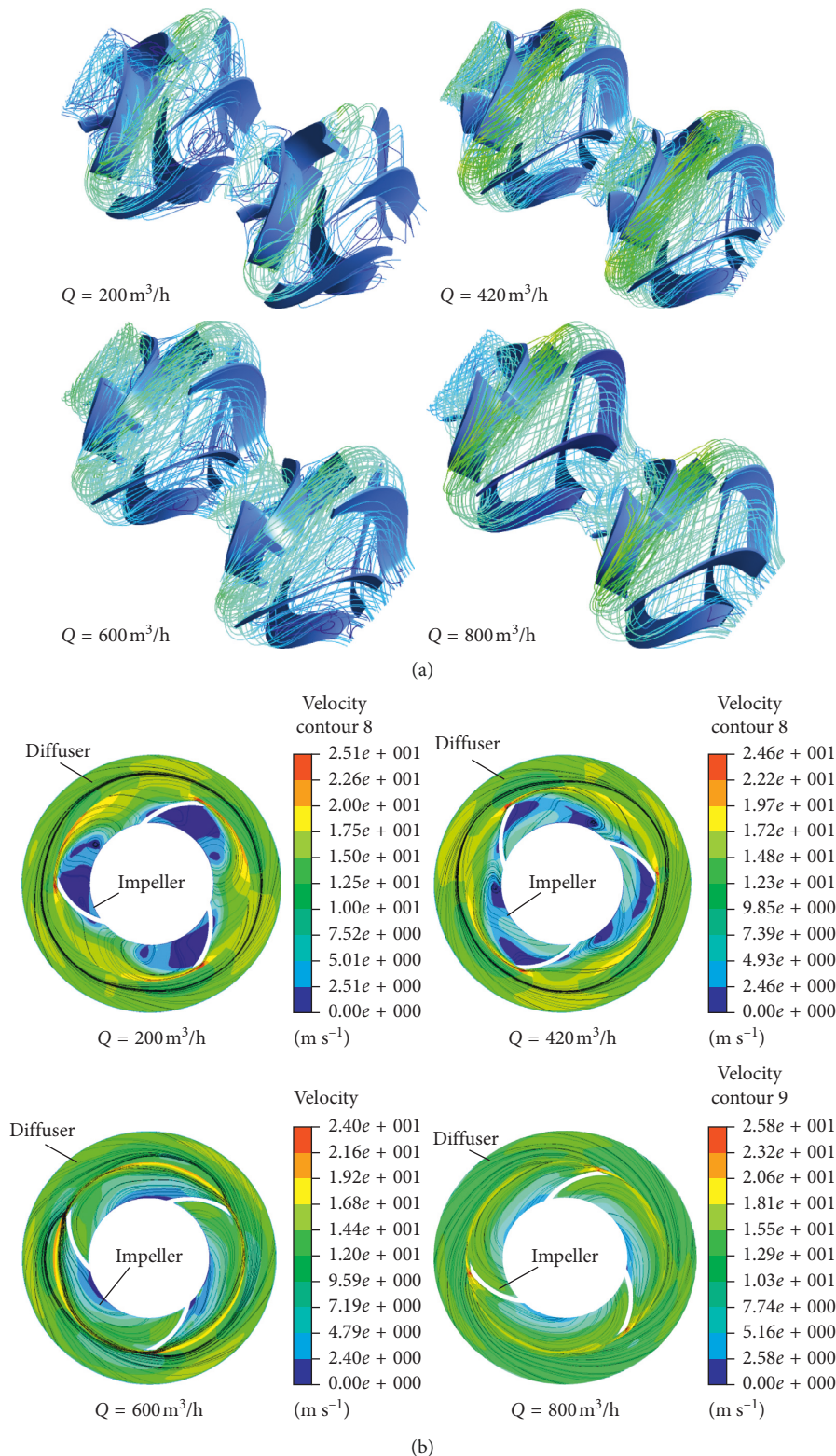
FIGURE 13: Streamline distribution for different flow rates (a) in the two-stage pump and (b) $z = 170$ mm.

blades. Therefore, the pressure pulsation period of the impeller is related to the number of diffuser blades, while the pressure pulsation period in the diffuser is related to the number of impeller blades.

Second, there was a certain difference in the frequency domain distribution between the first stage and the second stage diffuser, which may have been because the secondary impeller is not only affected by the secondary impeller but
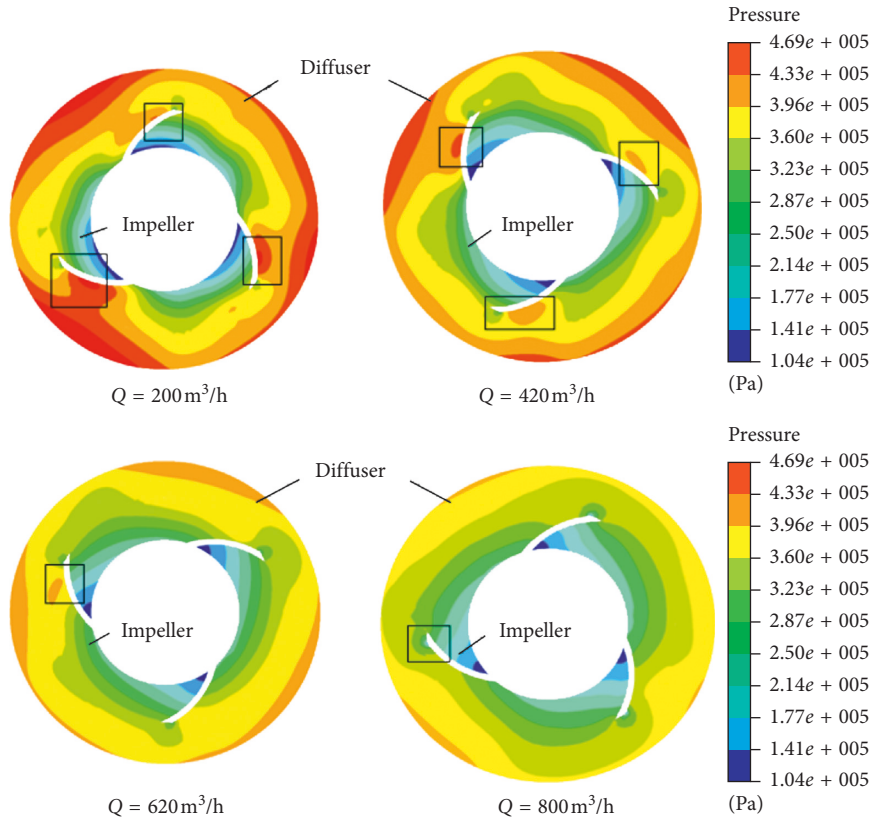
FIGURE 14: Static pressure distribution at $Z = 170$ mm for different flow rates.
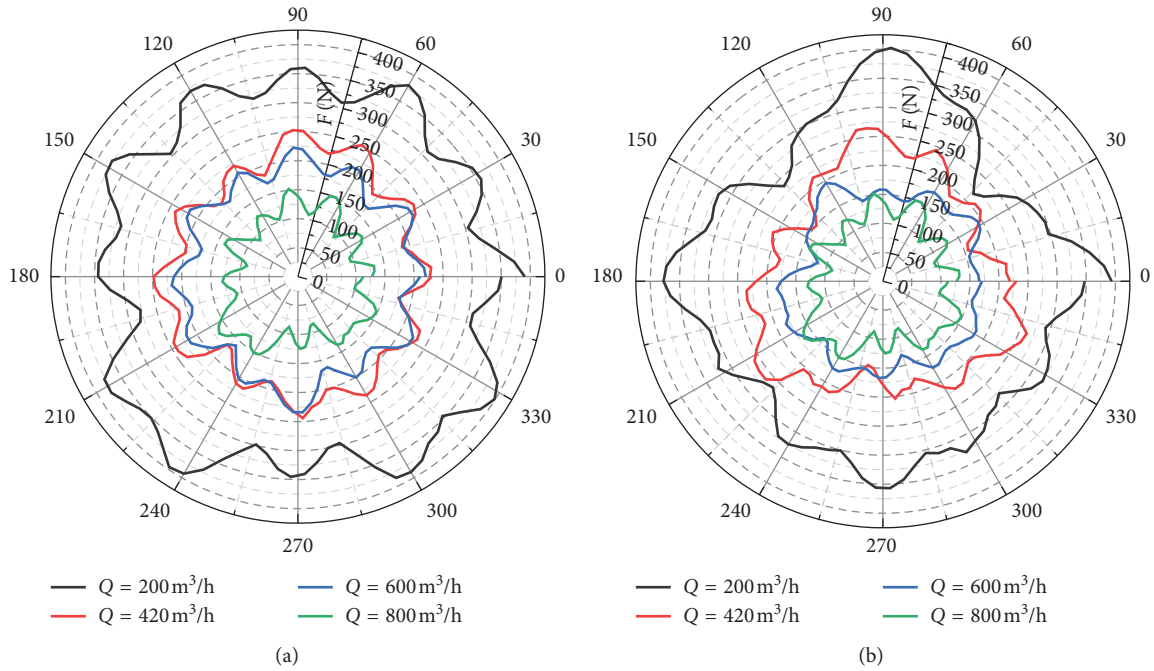

FIGURE 15: Polar coordinate diagrams of radial forces in the (a) primary impeller and (b) secondary impeller.
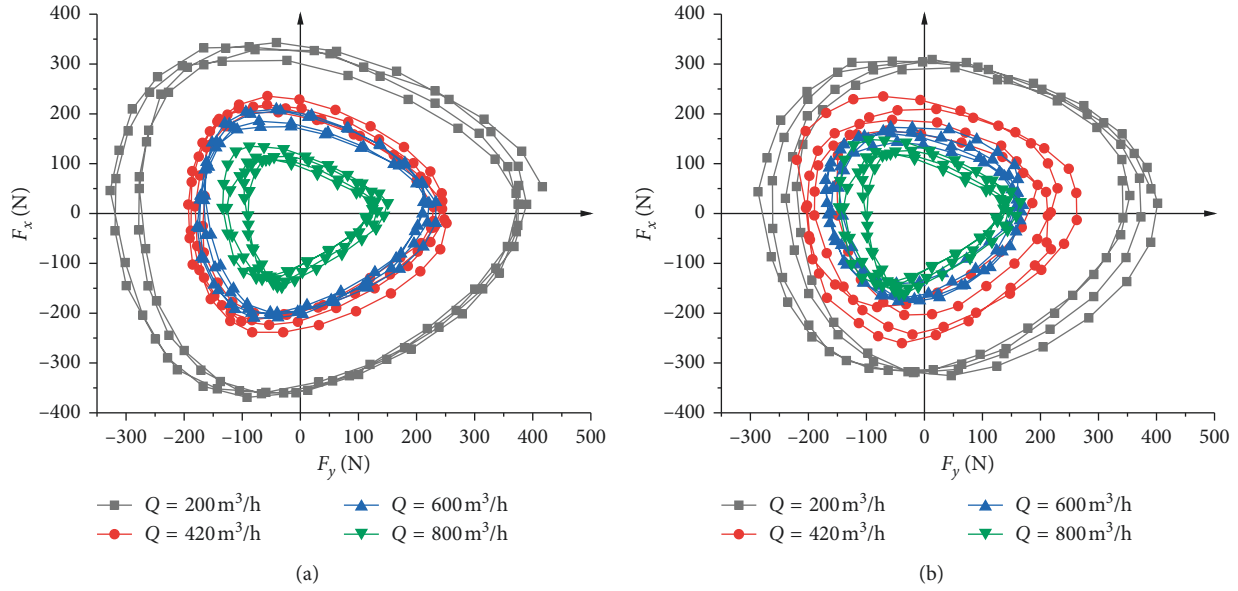
Figure 16: Radial force vector diagram in the (a) first-stage impeller and (b) second-stage impeller.

also affected by the grabbing flow channel; thus, the signal is superimposed. Another reason may have been the different outflow conditions of the primary and secondary diffusers.

Finally, the radial force was basically caused by the unstable pressure distribution at the impeller outlet. The flow asymmetry in the rotating impeller caused by the rotor-stator interference results in an unbalanced radial force. At the rated operating point, the radial force periodically fluctuates and the distribution of the vector diagram is also regular. When the flow rate is less than the rated point, the radial force fluctuation is very strong and unstable and the center of vector force distribution deviates from the axis. Therefore, considering the pump system stability, it is preferably avoided to operate at less than the rated condition for a long time period. The radial force acting on the secondary impeller is greater than that on the first impeller, and the fluctuation is more intense. It is not accurate to simulate the force acting on the impeller in a multistage pump using only one single-stage model.

Nomenclature

Q: Flow rate
Q_d: Design flow rate
Q_r: Rated flow rate
H: Head
S: Stage
n: Rotating speed
η: Hydraulic efficiency
D_1: Impeller inlet inlet diameter
D_2: Impeller outlet inlet diameter
D_3: Impeller inlet outlet diameter
D_4: Impeller outlet outlet diameter
D_5: Diffuser inlet inlet diameter
D_6: Diffuser outlet inlet diameter
D_7: Diffuser inlet outlet diameter
D_8: Diffuser outlet outlet diameter
b_2: Impeller outlet width
β_1: Impeller inlet blade angle
B_2: Impeller outlet blade angle
β_3: Diffuser inlet blade angle
β_4: Diffuser outlet blade angle
Z_1: Impeller blade number
Z_2: Diffuser blade number
P: Pressure
C_p: Pressure coefficient
ρ: Density
μ: Dynamic viscosity
μ_t: Turbulent viscosity
k: Turbulent kinetic energy
f_i: Impeller frequency
f_{ib}: Blade passing frequency
F: Radial force
n_s: The specific speed, $n_s = 3.65n\sqrt{Q}/H^{0.75}$.

Data Availability

The data used to support the findings of this study are included in the paper.

Conflicts of Interest

The authors declare that they have no conflicts of interest.

Acknowledgments

References

[1] Y. Nishi, "Static analysis of axially moving cables applied for mining nodules on the deep sea floor," *Applied Ocean Research*, vol. 34, pp. 45–51, 2012.

[2] Y. Shirayama, H. Itoh, and T. Fukushima, "Recent developments in environmental impact assessment with regard to mining of deep-sea mineral resources," *Deep-Sea Mining*, Springer International Publishing, New York, NY, USA, 2017.

[3] S. Liu, C. Liu, and Y. Dai, "Status and progress on researches and developments of deep ocean mining equipments," *Journal of Mechanical Engineering*, vol. 50, no. 2, pp. 8–18, 2014.

[4] W. S. Zou, Z. H. Li, and A. L. Chen, "Lifting motor pump in deep sea mining," *Journal of Central South University. Natural Science Edition*, vol. 42, no. 2, pp. 221–225, 2010.

[5] Y. Kang, S. Liu, W. Zou, H. Zhao, and X. Hu, "Design and analysis of an innovative deep-sea lifting motor pump," *Applied Ocean Research*, vol. 82, pp. 22–31, 2019.

[6] Z. Z. Sun, Y. M. Zhang, H. P. Xia, and S. S. Chen, "Radial force and pressure fluctuation analysis of axial flow pump rotor under different working conditions," *Journal of Irrigation and Drainage*, vol. 38, no. 1, pp. 122–128, 2019.

[7] W. Jiang, G. Li, P.-f. Liu, and L. Fu, "Numerical investigation of influence of the clocking effect on the unsteady pressure fluctuations and radial forces in the centrifugal pump with vaned diffuser," *International Communications in Heat and Mass Transfer*, vol. 71, no. 1, pp. 164–171, 2016.

[8] J. Gonzáles, C. Santolaria, J. L. Parrondo et al., "Unsteady radial forces on the impeller of a centrifugal pump with radial gap variation," in *Proceedings of the ASME/JSME 2003 4th Joint Fluids Summer Engineering Conference. Volume 1: Fora, Parts A, B, C, and D*, vol. 45, pp. 1173–1181, Honolulu, HI, USA, July 2003.

[9] S. Guo and H. Okamoto, "An experimental study on the fluid forces induced by rotor-stator interaction in a centrifugal pump," *The International Journal of Rotating Machinery*, vol. 9, no. 2, pp. 135–144, 2003.

[10] Y. B. Li, R. N. Li, X. R. Chen, W. G. Zhao, and L. X. Shen, "Numerical investigation of pressure fluctuation for a mixed flow pump impeller and vanes diffuser," *IOP Conference Series: Earth and Environmental Science*, vol. 15, no. 3, pp. 692–697, 2012.

[11] J. Feng, F. K. Benra, and H. J. Dohmen, "Numerical investigation on pressure fluctuations for different configurations of vaned diffuser pumps," *International Journal of Rotating Machinery*, vol. 2007, Article ID 34752, 10 pages, 2007.

[12] L. Zhou, W. D. Shi, W. G. Lu, H. Li, and B. Pei, "Analysis on pressure fluctuation of unsteady flow in deep-well centrifugal pump," *Transactions of the Chinese Society of Agricultural Engineering*, vol. 27, no. 10, pp. 44–49, 2011.

[13] P. Dupont, G. Caignaert, G. Bois et al., "Rotor-stator interactions in a vane-diffuser radial flow pump," in *Proceedings of ASME Fluids Engineering Division Summer Meeting*, pp. 1087–1094, Houston, TX, USA, October 2005.

[14] F. Shi and H. Tsukamoto, "Numerical study of pressure fluctuations caused by impeller-diffuser interaction in a diffuser pump stage," *Journal of Fluids Engineering*, vol. 123, no. 3, pp. 466–474, 2001.

[15] Z. Yao, "Experimental investigation of time-frequency characteristics of pressure fluctuations in a double-suction centrifugal pump," *Journal of Fluids Engineering*, vol. 133, no. 10, pp. 1076–1081, 2011.

[16] S. Anish, N. Sitaram, and H. D. Kim, "A numerical study of the unsteady interaction effects on diffuser performance in a centrifugal compressor," *Journal of Turbomachinery*, vol. 136, no. 1, pp. 253–256, 2013.

[17] A. Jaatinen, A. Grönman, T. Turunen-Saaresti, and J. Backman, "Effect of high negative incidence on the performance of a centrifugal compressor stage with conventional vaned diffusers," *Journal of Thermal Science*, vol. 20, no. 2, pp. 97–105, 2011.

[18] S. Q. Yuan and Y. Y. Ni, "Unsteady turbulent simulation and pressure fluctuation analysis for centrifugal pumps," *Chinese Journal of Mechanical Engineering*, vol. 22, no. 1, pp. 1–6, 2009.

[19] M. Solis, F. Bakir, and S. Khelladi, "Pressure fluctuations reduction in centrifugal pumps: influence of impeller geometry and radial gap," in *Proceedings of the ASME 2009 Fluids Engineering Division Summer Meeting. Volume 1: Symposia, Parts A, B and C*, pp. 253–265, American Society of Mechanical Engineers (ASME), Vail, CO, USA, August 2009.

[20] B. P. M. van Esch, "Performance and radial loading of a mixed-flow pump under non-uniform suction flow," *Journal of Fluids Engineering*, vol. 131, no. 5, pp. 36–40, 2009.

[21] R. Barrio, J. Fernández, E. Blanco, and J. Parrondo, "Estimation of radial load in centrifugal pumps using computational fluid dynamics," *European Journal of Mechanics-B/Fluids*, vol. 30, no. 3, pp. 316–324, 2011.

[22] J. Gonzalez, J. Fernandez, E. Blanco, and C. Santolaria, "Numerical simulation of dynanic effects due to impeller-volute intercaction in a centrifugal pump: pump analysis and design," *Journal of Fluids Engineering*, vol. 124, no. 2, pp. 348–355, 2002.

[23] M. Yang, S. Min, and F. J. Wang, "Pressure fluctuation characteristics of double volute pump and numerical simulation of radial force of impeller," *Journal of Agricultural Machinery*, vol. 40, no. 11, pp. 83–88, 2009.

[24] ANSYS, *ANSYS Academic Research, Release14.5, HelpSystem, CFX Documentation*, ANSYS, Inc., Canonsburg, PA, USA, 2002.

[25] M. G. Tan, R. Ding, H. L. Liu, and X. F. Wu, "Study on unsteady radial force characteristics in a dual-channel sewage pump," *Journal of Huazhong University of Science and Technology*, vol. 43, no. 12, pp. 42–47, 2015.

[26] W. D. Cao, G. H. Liu, W. D. Shi, and W. Dangxiong, "Distribution characteristics of unsteady pressure inside multistage centrifugal pump," *Transactions of the Chinese Society of Agricultural Engineering*, vol. 30, no. 14, pp. 64–70, 2014.

[27] X. Zhu, G. Li, W. Jiang, and L. Fu, "Experimental and numerical investigation on application of half vane diffusers for centrifugal pump," *International Communications in Heat and Mass Transfer*, vol. 79, pp. 114–127, 2016.

[28] Y. Y. Shi and Y. Z. Huang, "Numerical simulation of external characteristics of axial flow pump and comparative study of turbulence model," *Equipment Manufacturing Technology*, vol. 5, pp. 86–89, 2018.

[29] E. M. Ofuchi, H. Stel, T. Sirino et al., "Numerical investigation of the effect of viscosity in a multistage electric submersible pump," *Engineering Applications of Computational Fluid Mechanics*, vol. 11, no. 1, pp. 258–272, 2017.

[30] D. G. Duan, Z. M. Wei, X. Q. Jiang et al., "Technical differences between new and old standards for acceptance test of hydraulic performance of rotary power pumps," *Agricultural Engineering*, vol. 7, no. 6, pp. 139–141, 2017.

[31] H. W. Iversen, R. E. Rolling, and J. J. Carlson, "Volute pressure distribution Radial force on the impeller and volute

mixing losses of a radial flow centrifugal pump," *Journal of Engineering for Power*, vol. 82, no. 2, pp. 143-144, 1960.

[32] W. Y. Zhao, L. Zhang, and J. Luo, "Radial force numerical analysis of double suction centrifugal pump," *Irrigation and Drainage Machinery*, vol. 27, no. 4, pp. 205–209, 2009.